RESEARCH ARTICLE

QUANTUM SIMULATION

Realization of two-dimensional spin-orbit coupling for Bose-Einstein condensates

Zhan Wu,[1,2,3] Long Zhang,[1,4,5] Wei Sun,[1,2,3] Xiao-Tian Xu,[1,2,3] Bao-Zong Wang,[1,4,5] Si-Cong Ji,[1,2] Youjin Deng,[1,2,3] Shuai Chen,[1,2,3*] Xiong-Jun Liu,[4,5*] Jian-Wei Pan[1,2,3*]

Cold atoms with laser-induced spin-orbit (SO) interactions provide a platform to explore quantum physics beyond natural conditions of solids. Here we propose and experimentally realize two-dimensional (2D) SO coupling and topological bands for a rubidium-87 degenerate gas through an optical Raman lattice, without phase-locking or fine-tuning of optical potentials. A controllable crossover between 2D and 1D SO couplings is studied, and the SO effects and nontrivial band topology are observed by measuring the atomic cloud distribution and spin texture in momentum space. Our realization of 2D SO coupling with advantages of small heating and topological stability opens a broad avenue in cold atoms to study exotic quantum phases, including topological superfluids.

The spin-orbit (SO) interaction of an electron is a relativistic quantum mechanics effect that characterizes the coupling between the motion and spin of the electron when moving in an electric field. In the rest frame, the electron experiences a magnetic field proportional to the electron velocity and couples to its spin by the magnetic dipole interaction, rendering the SO coupling. The SO interaction plays an essential role in topological insulators, which have been predicted and experimentally discovered in two-dimensional (2D) and 3D materials (*1*, *2*), and topological superconductors (*3*, *4*), which host exotic zero-energy states called Majorana fermions (*5*) and still necessitate rigorous experimental verification. For topological insulators, the strong SO interaction leads to band inversion, which drives topological phase transitions in such systems. In superconductors, triplet p-wave pairing may occur when SO coupling is present and results in topologically nontrivial superconductivity under proper conditions (*6*).

Recently, there has been considerable interest in emulating SO effects and topological phases with cold atoms, driven by the fact that cold atoms can offer extremely clean platforms with full controllability to explore such exotic physics. In cold atoms, the synthetic SO interaction can be generated by Raman coupling schemes that flip atom spins and transfer momentum simultaneously (*7*, *8*); 1D SO interaction (*9*) has been successfully demonstrated in experiment for both cold boson (*10*, *11*) and fermion degenerate gases (*12*, *13*). With the 1D SO coupling, which corresponds to an Abelian gauge potential (*14*), one can study effects such as the magnetized or stripe ground states for bosons (*15*–*18*), spin dynamics (*19*, *20*), and 1D insulating topological states for fermions (*21*). Realizing higher dimensional SO couplings, which correspond to non-Abelian gauge potentials (*7*, *8*), can enable the study of a broader range of nontrivial quantum states such as topological insulators driven by 2D and 3D SO interactions (*1*, *2*). Furthermore, a 2D SO interaction is the minimal requirement to reach a gapped topological superfluid phase through a conventional s-wave superfluid state (*22*, *23*).

Several schemes have been proposed for generating 2D and 3D SO couplings (*7*, *8*, *24*–*26*). Notable progress was recently achieved when 2D SO couplings were demonstrated for pseudospins defined by two dark states in an empty tripod system (*27*). However, realizing 2D SO coupling for quantum degenerate atom gases remains challenging. Very recently, it was proposed that 2D SO coupling can be realized by a simple optical Raman lattice scheme that applies two pairs of light beams to create the lattice and Raman potentials simultaneously (*28*). However, this scheme requires the challenging realization of two Raman transitions with a locked relative phase. Here we propose a minimal scheme that overcomes these challenges and realizes 2D SO coupling with ^{87}Rb Bose-Einstein condensates (BECs).

[1]Shanghai Branch, National Laboratory for Physical Sciences at Microscale and Department of Modern Physics, University of Science and Technology of China, Shanghai 201315, China. [2]Chinese Academy of Sciences (CAS) Center for Excellence and Synergetic Innovation Center of Quantum Information and Quantum Physics, University of Science and Technology of China, Hefei, Anhui 230026, China. [3]CAS-Alibaba Quantum Computing Laboratory, Shanghai 201315, China. [4]International Center for Quantum Materials, School of Physics, Peking University, Beijing 100871, China. [5]Collaborative Innovation Center of Quantum Matter, Beijing 100871, China.
*Corresponding author. Email: shuai@ustc.edu.cn (S.C.); xiongjunliu@pku.edu.cn (X.-J.L.); pan@ustc.edu.cn (J.-W.P.)

Theoretical proposal

We aim to realize 2D SO coupling and topological band for ultracold atoms on a square lattice with the Hamiltonian

$$H = \left[\frac{\hbar^2\mathbf{k}^2}{2m} + V_{\text{latt}}(x,z)\right]\otimes\mathbf{1} + \mathcal{M}_x(x,z)\sigma_x + \mathcal{M}_y(x,z)\sigma_y + m_z\sigma_z \quad (1)$$

where ħ is Planck's constant h divided by 2π, $\mathbf{k}$ is the wave vector that represents the momentum of the atoms, $\mathbf{1}$ is the 2-by-2 unit matrix, $\sigma_{x,y,z}$ are Pauli matrices acting on the spins, m is the mass of an atom, V_{latt} denotes the lattice potential in the xz plane, $\mathcal{M}_{x,y}$ are periodic Raman coupling potentials, and m_z is a tunable Zeeman constant. The lattice potential V_{latt} is spin-independent and can induce nearest-neighbor hopping that conserves the atom spin, whereas $\mathcal{M}_{x,y}$ induce hopping that flips atom spin. This is different from the laser-assisted tunneling scheme without spin-flip (*29*–*31*). The overall effect of hopping along $\hat{x}$ and $\hat{z}$ directions results in 2D SO coupling, which can lead to nontrivial topological bands for the square lattice.

Here we propose to realize the Hamiltonian (Eq. 1) through a minimal scheme, which is generic and applicable to both boson and fermion atoms. Figure 1 illustrates the realization in a ^{87}Rb Bose gas, with $|\uparrow\rangle \equiv |1,-1\rangle$ and $|\downarrow\rangle \equiv |1,0\rangle$; the hyperfine state $|1,+1\rangle$ can be removed by a sufficiently large two-photon detuning. The minimal ingredients of the realization include a blue-detuned square lattice created with two light components denoted by the blue lines, and the periodic Raman potentials generated together with additional light components denoted by the red lines (Fig. 1A). Both ingredients can be achieved with a single in-plane (xz) linearly polarized laser source. The initial phases of the light beams have no effect on this optical Raman lattice scheme (*32*), and we neglect them in the following discussion. The optical lattice is generated by E_{1x} and E_{1z} (blue lines), which are incident from horizontal (x) and vertical (z) directions, respectively (Fig. 1A), and can be created from a single light of frequency ω_1 by a beam splitter. The beams are reflected by two mirrors (M_1 and M_2) and form standing waves in the intersecting area described by $\mathbf{E}_{1x} = \hat{z}\bar{E}_{1x}e^{i\varphi_L/2}\cos(k_0x - \varphi_L/2)$ and $\mathbf{E}_{1z} = \hat{x}\bar{E}_{1z}e^{i\varphi_L/2}\cos(k_0z - \varphi_L/2)$, where $\bar{E}_{1x/1z}$ are amplitudes and the phase $\varphi_L = k_0L$ is acquired through the optical path L from the intersecting point to mirror M_1, then to M_2, and back to the intersecting point, with $k_0 = \omega_1/c$. For alkali atoms, we can show that the optical potential generated by linearly polarized lights is spin-independent when the detuning Δ is much larger than the hyperfine structure splittings (*32*). The lattice potential then takes the form

$$V_{\text{latt}}(x,z) = V_{0x}\cos^2(k_0x - \varphi_L/2) + V_{0z}\cos^2(k_0z - \varphi_L/2) \quad (2)$$

where $V_{0x/0z} = \hbar|\Omega_{x/z}|^2/\Delta$. The Rabi frequency amplitudes of the standing waves $\Omega_{x/z} \equiv \mathbf{d}_{\text{eff}}\cdot\bar{\mathbf{E}}_{1x/1z}/\hbar$, where $\overline{\mathbf{E}}_{1x/1z} = \overline{E}_{1x/1z}\hat{z}/\hat{x}$; and the effective dipole matrix $\mathbf{d}_{\rm eff}$ takes into account the transitions from a ground state $(g_{\uparrow,\downarrow})$ to all relevant excited states in D_1 and D_2 lines (Fig. 1B). The lattice potential induces spin-conserved hopping, as illustrated in Fig. 1D.

The Raman couplings are induced when another beam E_{2z} of frequency ω_2 is incident from the z direction. The light components E_{1z} and E_{2z} can be generated from a single laser source via an acoustic-optic modulator (AOM), which controls their frequency difference $\delta\omega = \omega_1 - \omega_2$ and amplitude ratio $\overline{E}_{2z}/\overline{E}_{1z}$. The light E_{2z} generates plane-wave fields $\mathbf{E}_{2z} = \hat{x}\overline{E}_{2z}e^{ik_0z}$ and $\mathbf{E}_{2x} = \hat{z}\overline{E}_{2x}e^{i(-k_0x+\varphi_{\rm L}-\delta\varphi_{\rm L})}$, where the irrelevant initial phase is neglected (*32*). The relative phase $\delta\varphi_{\rm L} = L\delta\omega/c$, acquired by E_{2x}, is a crucial parameter, which can be precisely manipulated by changing the optical path L or $\delta\omega$, and it controls the dimensionality of the realized SO coupling. The standing-wave and plane-wave beams form a double-Λ type configuration (Fig. 1C), with E_{1x} and E_{2z} generating one Raman potential via $|F,0\rangle$ in the form $M_{0x}\cos(k_0x-\varphi_{\rm L}/2)e^{i(k_0z-\varphi_{\rm L}/2)}$, and E_{1z} and E_{2x} producing another one via $|F,-1\rangle$ as $M_{0y}\cos(k_0z-\varphi_{\rm L}/2)e^{-i(k_0x-\varphi_{\rm L}/2)-i\delta\varphi_{\rm L}}$. Note that lattice sites of a blue-detuned lattice are located around zeros of optical fields. It follows that terms such as $\cos(k_0x-\varphi_{\rm L}/2)\cos(k_0z-\varphi_{\rm L}/2)$, which is antisymmetric with respect to each site in both x and z directions, have small contribution to low-band physics. Neglecting such terms yields

$$\mathcal{M}_x(x,z) = M_x - M_y\cos\delta\varphi_{\rm L} \qquad (3)$$

$$\mathcal{M}_y(x,z) = M_y\sin\delta\varphi_{\rm L} \qquad (4)$$

Here $M_{x/y} = M_{0x/y}\cos(k_0x/z-\varphi_{\rm L}/2)\sin(k_0z/x-\varphi_{\rm L}/2)$, with $M_{0x}/M_{0y} = \overline{E}_{1x}\overline{E}_{2z}/(\overline{E}_{1z}\overline{E}_{2x})$ (*32*). Together with an effective Zeeman term $(m_z = \hbar\delta/2)$, which is controlled by tuning the two-photon detuning δ (Fig. 1C), we reach the effective Hamiltonian (Eq. 1). Note that M_x (M_y) is antisymmetric with respect to each lattice site along the $\hat{x}(\hat{z})$ direction (Fig. 1, E and F). This feature has an important consequence that M_x (M_y) leads to spin-flipped hopping only along x (z) direction. Moreover, the phase difference $\delta\varphi_{\rm L}$ governs the relative strength of the σ_x and σ_y terms and thus determines the dimensionality of the SO coupling. For example, setting $\delta\omega$ = 50 MHz yields $\delta\varphi_{\rm L} = \pi/2$ for L = 1.5 m, resulting in optimal 2D SO coupling. Further increasing the optical path to L = 3.0 m gives $\delta\varphi_{\rm L} = \pi$, and the SO coupling becomes 1D. This enables a fully controllable study of the crossover between 2D and 1D SO couplings by tuning $\delta\varphi_{\rm L}$ and provides a comparison measurement to confirm the realization of 2D SO interaction.

2D SO coupling and topological band

The Hamiltonian (Eq. 1) has an inversion symmetry defined by $(\sigma_z\otimes R_{\rm 2D})H(\sigma_z\otimes R_{\rm 2D})^{-1} = H$, where the 2D spatial operator $R_{\rm 2D}$ transforms the Bravais lattice vector $\mathbf{R}\to-\mathbf{R}$. For the s-band, the Bloch Hamiltonian is given by $\mathcal{H}(\mathbf{q}) = [m_z - 2t_0(\cos q_xa + \cos q_za)]\sigma_z + 2t_{\rm so}\sigma_y\sin q_xa + 2t_{\rm so}\,\sigma_x\sin q_za$, which, around the Γ point, takes the form $\mathcal{H}(\mathbf{q}) = [m_z - 4t_0 + t_0a^2(q_x^2+q_z^2)]\sigma_z + \lambda_{\rm so}q_x\sigma_y + \lambda_{\rm so}q_z\sigma_x$, with the SO coefficient $\lambda_{\rm so} = 2at_{\rm so}$ being tunable by varying Raman coupling strength (*32*), unlike in the previous schemes (*10–13*, *27*). Here, t_0 and $t_{\rm so}$ denote the spin-conserved and spin-flip hopping coefficients, respectively, and a is the lattice constant. This is a quantum anomalous Hall model driven by SO coupling (*28*), which cannot be exactly realized in solid-state materials. It was shown (*33*) that the topology of inversion symmetric Chern bands can be determined by the product of the spin-polarizations $P(\Lambda_j)$ at four highly symmetric momenta $\Theta = \Pi_{j=1}^{4}{\rm sgn}[P(\Lambda_j)]$, with the momenta $\{\Lambda_j\} = \{{\rm G}(0,0), X_1(0,\pi), X_2(\pi,0), M(\pi,\pi)\}$. The topological (or trivial) phase corresponds to $\Theta = -1$ (or +1). Two typical examples are shown in Fig. 2 by exactly diagonalizing H, with $V_{0x,z} = 5E_{\rm r}$, $M_{0x,y} = 1.2E_{\rm r}$, $\delta\varphi_{\rm L} = \pi/2$, and $m_z = 0.1E_{\rm r}$ (Fig. 2, A, B, E, and F) or $m_z = 0.4E_{\rm r}$ (Fig. 2, C and D), where the recoil energy is $E_{\rm r} = \hbar^2k_0^2/2m$. For the chosen parameters, the lowest two subbands are gapped (Fig. 2, A to D). When $m_z = 0.1E_{\rm r}$, the spin polarizations at the Γ and M points are opposite (Fig. 2, B, E, and F), implying that the band is topologically nontrivial. In contrast, the polarizations are the same for $m_z = 0.4E_{\rm r}$ (Fig. 2D), and the band is trivial.

The present scheme displays several essential advantages: (i) Fluctuations, such as those caused by the mirror oscillations, have a tiny effect on L and, thus, do not affect $\delta\varphi_{\rm L}$ appreciably. The initial phases of light beams globally shift the optical Raman lattice but cannot affect the relative configuration between $V_{\rm latt}$ and the Raman

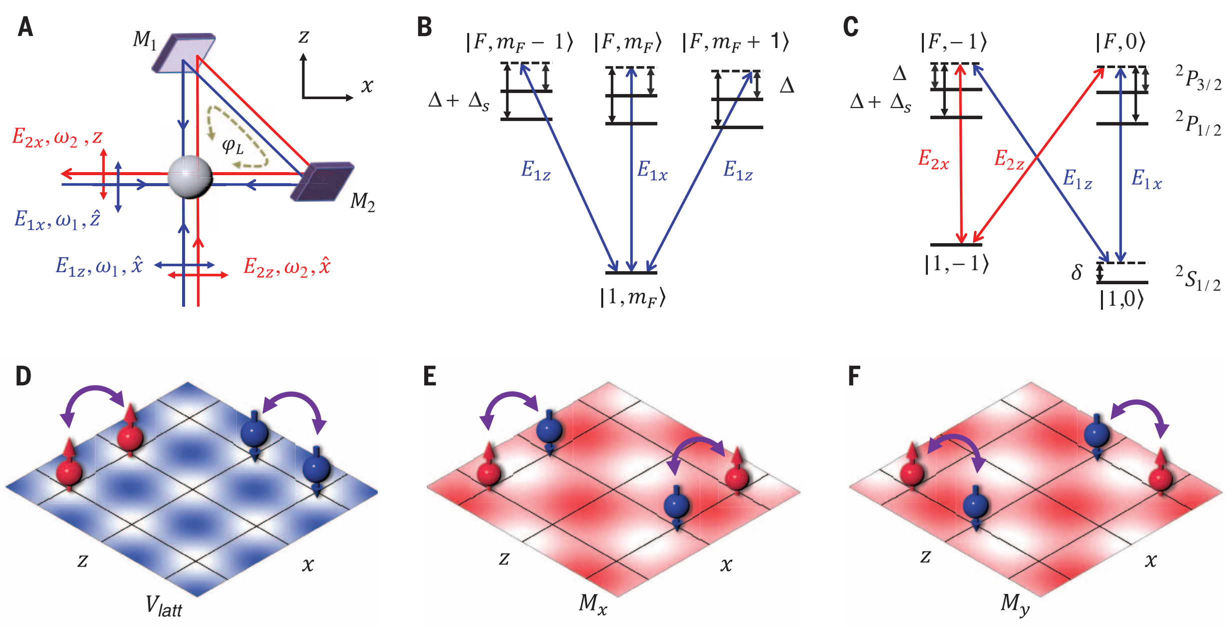

Fig. 1. Proposal of the optical Raman lattice scheme. (**A**) Sketch of the setup for realization. The light components $E_{1x,1z}$ (blue lines) form a spin-independent square optical lattice in the intersecting area and generate two periodic Raman potentials, together with the light components $E_{2x,2z}$ (red lines). (**B**) Optical transitions to generate lattice potentials by $E_{1x,1z}$ for the states $|1,m_{\rm F}\rangle$ $(m_{\rm F} = 0,-1)$, with $|\uparrow\rangle = |1,-1\rangle$ and $|\downarrow\rangle = |1,0\rangle$, including all relevant D_1 and D_2 transitions. Here, F is the quantum number of hyperfine states, $m_{\rm F}$ is the quantum number of magnetic substates, and $\Delta_{\rm s}$ denotes the fine-structure splitting. (**C**) Two periodic Raman potentials are generated through a double-Λ type configuration by $E_{1x,2z}$ and $E_{1z,2x}$, respectively. (**D** to **F**) Profiles of lattice potential for $V_{0x} = V_{0z} = 5E_{\rm r}$ (D) and Raman potentials M_x (E) and M_y (F) for $M_{0x} = M_{0y} = 1.2E_{\rm r}$. The color intensity characterizes the relative height of the potentials. The Raman potentials M_x and M_y are antisymmetric (or symmetric) with respect to the lattice site along the x (or z) and z (or x) directions, respectively.

potentials (32). Thus, the present scheme is intrinsically immune to any phase fluctuations in the setting, which avoids the need for phase-locking, a challenging task in practical realizations. (ii) As long as $\overline{E}_{1x} = \overline{E}_{1z}$ and $\overline{E}_{2x} = \overline{E}_{2z}$, which are easily accomplished, the system becomes uniform in the x and z directions: $V_{0x} = V_{0z}$ and $M_{0x} = M_{0y}$. No fine-tuning of optical potentials is required. (iii) All of the coupling beams can be created from only a single laser source, simplifying the experimental layout. (iv) Compared with the generation of 1D SO coupling, the present double-Λ Raman configuration (Fig. 1C) does not suffer additional instability or heating in the realization. These advantages render the present scheme immediately feasible in ultracold atom experiments with the current technology.

Experimental setup

In our experiment, a BEC of about 1.5×10^5 ^{87}Rb atoms in the state $|1,-1\rangle$ is prepared in a crossed optical dipole trap with trapping frequencies of $\{\omega_x, \omega_y, \omega_z\} = 2\pi \times \{45, 45, 55\}$Hz, which can suppress the antitrapping effect of blue detuned lights. A bias magnetic field of 49.6 G is applied along the $\hat{z}$ direction to generate the Zeeman splitting and determine the quantization axis. As shown in Fig. 3A, three laser beams (wavelength = 767 nm) in the xz plane illuminate the atoms for the generation of the Hamiltonian (Eq. 1). Among these laser beams, a pair of counterpropagating lasers with the same frequency ω_1 (the blue lines in Fig. 3A labeled as "lattice lasers") produces the two-dimensional optical lattice. These two lasers are incident along the $\hat{x}$ and $\hat{z}$ directions, respectively, and are reflected by two mirrors (M_1 and M_2) to form the standing waves in both directions. The polarizations are set in the xz plane so that the interference between the $\hat{x}$ and $\hat{z}$ directions is automatically avoided. The third laser with frequency ω_2 (the red line in Fig. 3A labeled as "Raman laser") is a running wave, which is incoming along the $\hat{z}$ direction with the same polarization as the lattice lasers. All three laser beams are generated from the same Ti:sapphire laser, and the frequencies and amplitudes of these beams are controlled by two phase-locked AOMs. Thus, the phase coherence is automatically kept, and no additional phase-locking is needed. The Raman and lattice lasers are also coupled into the same optical fiber and then lead to the science chamber, which helps to avoid the phase noise due to the imperfect overlap in propagation. The frequency difference $\omega_1 - \omega_2$ is set to 35 MHz to match the Zeeman splitting between the $|1,-1\rangle$ and $|1,0\rangle$ states. The $|1,1\rangle$ state is effectively suppressed because of a large quadratic Zeeman splitting, and the system can be treated as a two-level system. The detuning m_z can be adjusted by tuning the bias magnetic field. By controlling the intensities of the lattice and Raman lights, we set the lattice depth as $V_{0x} = V_{0z}$ and the Raman coupling strength as $M_{0x} = M_{0y}$.

In the experiment, the BEC is first prepared in the dipole trap with the bias magnetic field being switched on. Then, the intensities of the lattice and the Raman beams are simultaneously ramped up to the setting value in 40 ms. As a consequence, the BEC atoms are adiabatically loaded in the local minimum of the lowest band at the Γ point. The phase difference $\delta\varphi_L$ in the Hamiltonian can be achieved by setting the propagating length between the two mirrors M_1 and M_2. The detection is performed in the same way as described in (11, 18, 34). The spin-resolved time-of-flight (TOF) imaging is taken after all laser beams and the bias magnetic field are suddenly turned off and the gas has expanded freely for 24 ms within a gradient magnetic field to resolve both the momentum and spin.

Experimental results

To demonstrate the realization of 2D SO coupling, we study the crossover effect in the BEC regime by tuning $\delta\varphi_L$. At $m_z = 0$ and by preparing the atoms in the spin-up state, we can adiabatically load the ^{87}Rb condensate into the Γ point. Then, we perform the spin-resolved TOF expansion, which projects Bloch states onto free momentum states with fixed spin polarizations. Figure 3B shows the TOF images for various values of $\delta\varphi_L$. For the spin-up ($|\uparrow\rangle$) state, five atom clouds are observed: The major portion of the BEC cloud remains at momentum $(k_x, k_z) = (0, 0)$, whereas four small fractions are transferred to momenta $(\pm 2k_0, 0)$ and $(0, \pm 2k_0)$ by the first-order transitions due to the lattice potential V_{latt}. Depending on $\delta\varphi_L$, two or four small BEC clouds are formed in the $|\downarrow\rangle$ state at the diagonal corners with momenta $(\pm k_0, \pm k_0)$. This is a consequence of SO coupling; the atom clouds are generated by the Raman

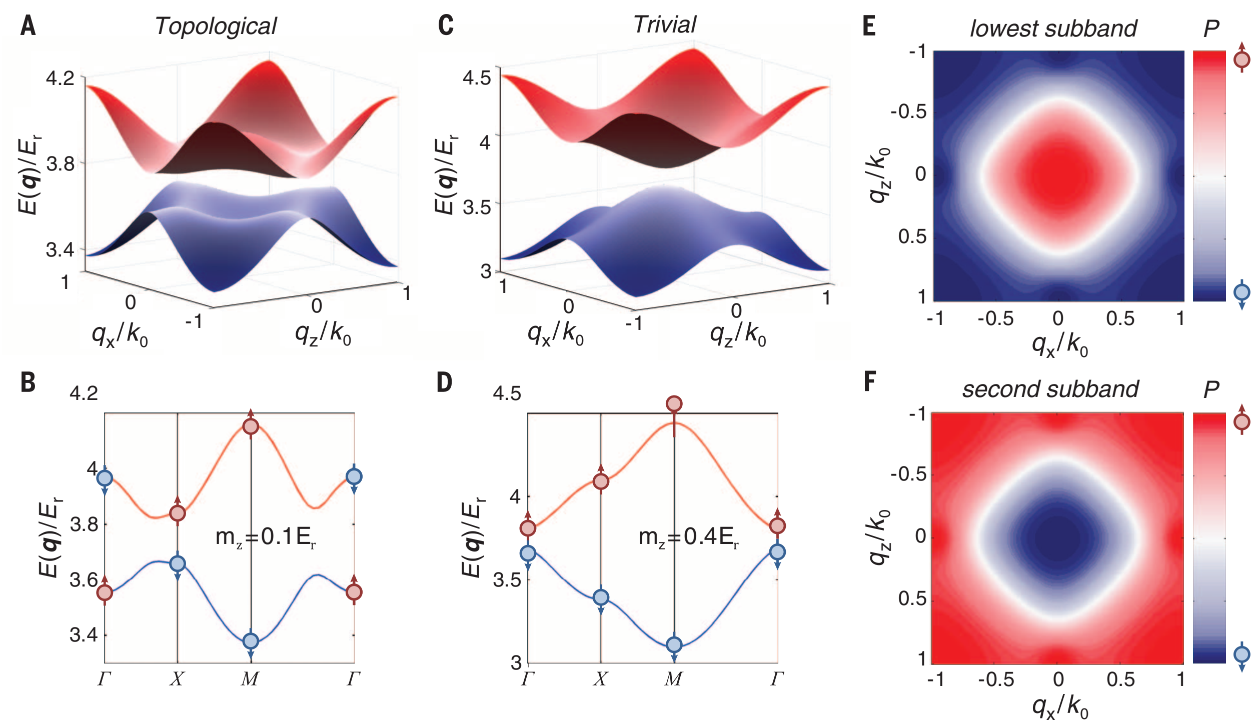

Fig. 2. Band structure and spin texture with 2D SO interaction. This figure shows an example of gapped band structure with nontrivial band topology (**A**), spin texture along the loop Γ-X-M-Γ (**B**), and spin polarization distributions $\langle\sigma_z\rangle$ of the lowest band (**E**) and the second band (**F**) for $m_z = 0.1E_r$. (**C** and **D**) Example of a trivial band with gapped band structure (C) and spin texture along the loop Γ-X-M-Γ (D) for $m_z = 0.4E_r$. For all panels, we take $V_{0x} = V_{0z} = 5E_r$, $M_{0x} = M_{0y} = 1.2E_r$, and $\delta\varphi_L = \pi/2$.

transitions, which flip spin and transfer momenta of magnitude $\sqrt{2}k_0$ along the diagonal directions. As given in Eqs. 3 and 4, the Raman terms $\mathcal{M}_x$ and $\mathcal{M}_y$ depend on $\delta\varphi_L$. For $\delta\varphi_L = \pi/2$, four small clouds in the $|\downarrow\rangle$ state with TOF momentum $\vec{k} = (\pm k_0, \pm k_0)$ are observed (Fig. 3B), reflecting the 2D SO coupling. On the other hand, by tuning the relative phase to $\delta\varphi_L = 3\pi/4$, the population of atom clouds in the two diagonal directions becomes imbalanced. Furthermore, the system reduces to 1D SO couplings when $\delta\varphi_L = \pi$ and 2π, with $\mathcal{M}_x = M_x \pm M_y$ and $\mathcal{M}_y = 0$. In this case, the Raman pumping generates only a single diagonal pair of BEC clouds, as shown in Fig. 3B for $\delta\varphi_L = \pi, 2\pi$. This is similar to the 1D SO coupling in the free space in (*11*), where the Raman coupling flips the atom spin and generates a pair of atom clouds with opposite momenta. Figure 3B also shows that there is a difference of distribution between the lower left and upper right BEC clouds at $|\downarrow\rangle$, which is due to non–tight-binding correction. A simple analysis reveals that although the fully antisymmetric Raman terms $\cos(k_0x + \alpha)\cos(k_0z + \beta)$ have negligible effects in the tight-binding limit of the lattice, they give finite contributions in the moderate lattice regime and are responsible for such difference of distribution (*32*). To quantify the crossover effect, we define $W = (\mathcal{N}_{\hat{x}-\hat{z}} - \mathcal{N}_{\hat{x}+\hat{z}})/(\mathcal{N}_{\hat{x}-\hat{z}} + \mathcal{N}_{\hat{x}+\hat{z}})$ to characterize the imbalance of the Raman coupling–induced atom clouds, with $\mathcal{N}_{\hat{x}\pm\hat{z}}$ denoting the atom number of the two BEC clouds along the diagonal $\hat{x}\pm\hat{z}$ direction. W can be fitted by a simple cosine curve $\cos\delta\varphi_L$ (Fig. 3C), reflecting the crossover between the 2D and 1D SO couplings realized in the present BEC regime.

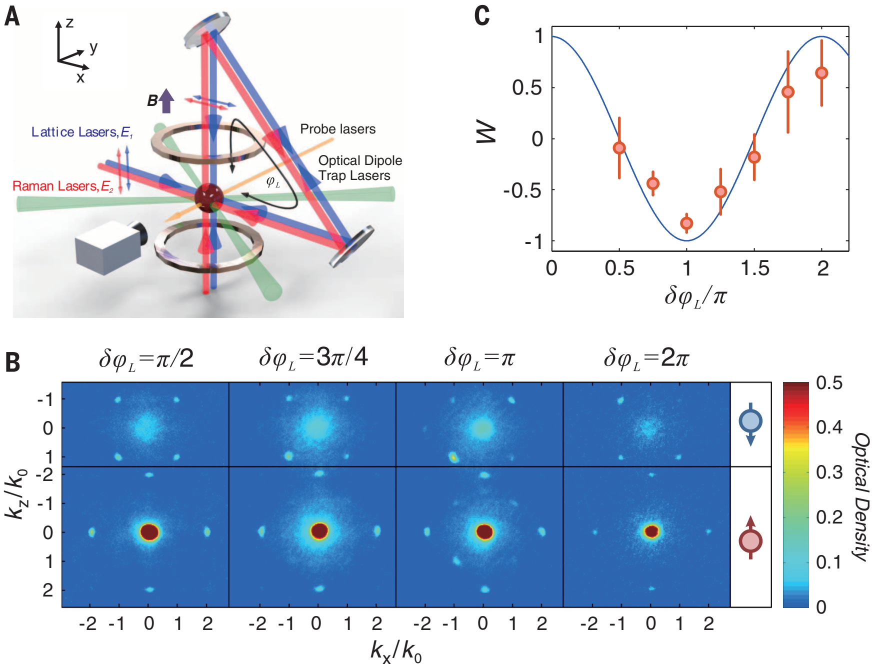

Fig. 3. Experimental realization of 2D SO interaction and 1D-2D crossover. (**A**) Experimental setup. ***B*** is the biased magnetic field, which generates the Zeeman splitting and gives the quantum axis of the atoms. (**B**) Spin-resolved TOF images of BEC atoms for $\delta\varphi_L = \pi/2$, $\delta\varphi_L = 3\pi/4$, $\delta\varphi_L = \pi$, and $\delta\varphi_L = 2\pi$. The other parameters are measured as $V_{0x} = V_{0z} = 4.16E_r$, $M_{0x} = M_{0y} = 1.32E_r$, and $m_z = 0$. (**C**) Measured imbalance W between the Raman coupling–induced atoms in the two diagonal directions as a function of the relative phase $\delta\varphi_L$, compared to a cosine curve $\cos\delta\varphi_L$. The results are averaged over ~30 TOF images.

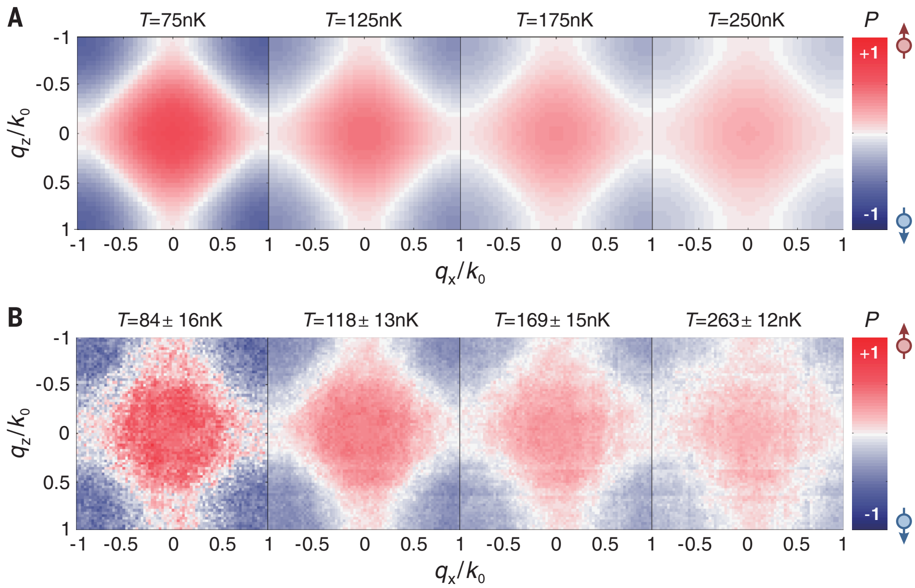

Fig. 4. Spin texture at different temperatures with $\delta\varphi_L = \pi/2$. (**A**) Numerical calculations for temperatures T = 250, 175, 125, and 75 nK. P is the polarization of the atomic spin, where +1 means spin up and −1 means spin down. (**B**) Experimental measurements of spin polarization at different measured temperatures. Parameters for the numerical calculation are the same as the experimental parameters: $V_{0x} = V_{0z} = 4.16E_r$, $M_{0x} = M_{0y} = 1.32E_r$, and $m_z = 0$.

Next, we focus on the 2D isotropic SO coupling with $\delta\varphi_L = \pi/2$, measure the spin distribution in the first Brillouin zone, and detect the topology of the bands by varying the bias magnetic field to tune δ, which governs m_z. For this purpose, we need a cloud of atoms with a temperature such that the lowest band is occupied by a sufficient number of atoms, whereas the population of atoms in the higher bands is small. A similar procedure used in the above BEC measurement is followed, except that the atoms are cooled to relatively higher temperatures, which are measured a posteriori using the momentum distribution of hot atoms. After a TOF expansion, we obtain the atom distributions of both spin-up and spin-down states in the momentum space and then map them back to the Bloch momentum space according to the plane-wave expansion of eigenfunctions. We define the spin polarization $P(\mathbf{q}) = [n_\uparrow(\mathbf{q}) - n_\downarrow(\mathbf{q})]/[n_\uparrow(\mathbf{q}) + n_\downarrow(\mathbf{q})]$, with $n_{\uparrow,\downarrow}(\mathbf{q})$ being the density of atoms of the corresponding spin state in the first Brillouin zone. Figure 4, A and B, shows the numerical results and experimentally measured spin polarizations at different temperatures, respectively, for $m_z = 0$, $V_{0x} = V_{0z} = 4.16E_r$, and $M_{0x} = M_{0y} = 1.32E_r$. In performing numerical simulation, the finite temperature effect is taken into account based on the Bose-Einstein statistics $f(E) = 1/[e^{(E_q - \mu/k_B T)} - 1]$, with k_B the Boltzmann constant and E_q given by band energies of the Hamiltonian (Eq. 1), plus the kinetic energy $\hbar^2 q_y^2/2m$ due to the motion in the out-of-lattice plane (y) direction. The average atom density is taken as $n = 3 \times 10^{19}\ \mathrm{m}^{-3}$, which determines the chemical potential μ. There is good agreement between the theoretical and experimental results, which demonstrates the feasibility and reliability of the spin polarization measurement. Furthermore, the results in Fig. 4 suggest that a temperature around T = 100 nK is optimal to extract

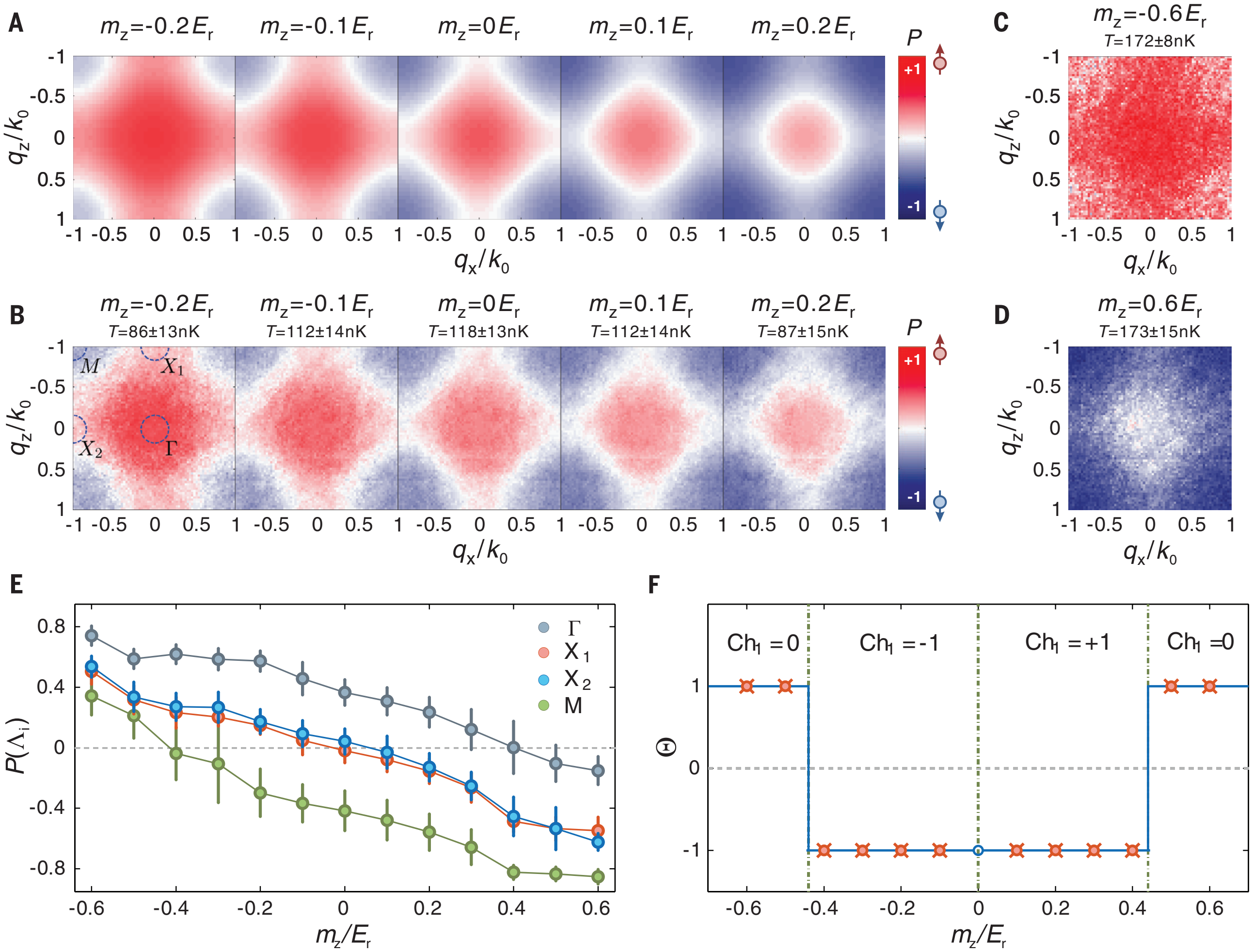

Fig. 5. Spin texture and band topology with $\delta\varphi_L = \pi/2$. (**A** and **B**) Spin texture at different m_z by tuning the two-photon detuning. Experimental measurements (B) are compared to numerical calculations at T = 100 nK (A). (**C** and **D**) Measured spin texture in topologically trivial bands at $m_z = -0.6E_r$ (C) and $m_z = 0.6E_r$ (D). (**E** and **F**) Measured spin polarization $P(\Lambda_j)$ at the four symmetric momenta $\{\Lambda_j\} = \{\Gamma, X_1, X_2, M\}$ as a function of m_z (E), and the product $\Theta = \Pi_{j=1}^{4}\mathrm{sgn}[P(\Lambda_j)]$ (F), which determines the Chern number Ch_1 and characterizes the topology of the band. In all the cases, we set $V_{0x} = V_{0z} = 4.16E_r$ and $M_{0x} = M_{0y} = 1.32E_r$.

the spin-texture information of the lowest band. In comparison, if the temperature is too high, atoms are distributed over several bands and the visibility of the spin polarization will be greatly reduced, whereas too low a temperature can also reduce the experimental resolution because the atoms will be mostly condensed at the band bottom.

We then measure the spin polarization as a function of detuning m_z to reveal the topology of the lowest-energy band, with $V_{0x} = V_{0z} = 4.16E_r$ and $M_{0x} = M_{0y} = 1.32E_r$. The numerical calculations and TOF-measured images of $P(\mathbf{q})$ are in agreement (Fig. 5A and Fig. 5, B to D, respectively). In Fig. 5E, we plot the values of polarization $P(\Lambda_j)$ for the four highly symmetric momenta Γ, X_1, M, and X_2. $P(X_1)$ and $P(X_2)$ always have the same sign, whereas the signs of $P(\mathrm{G})$ and $P(M)$ are opposite for small $|m_z|$ and the same for large $|m_z|$, with a transition occurring at the critical value of $|m_z^c|$ that is a bit larger than $0.4E_r$. At transition points, the spin polarization $P(X_1)$ or $P(X_2)$ vanishes due to the gap closing and thermal equilibrium. From the measured spin polarizations, the product Θ and the corresponding Chern number, given by $\mathrm{Ch}_1 = -\frac{1-\Theta}{4}\sum_{j=1}^{4}\mathrm{sgn}[P(\Lambda_j)]$ (*32*, *33*), can be read off (Fig. 5F). A numerical calculation using exact diagonalization (*32*) in the present experimental parameter regime can show two transitions between the topologically trivial and nontrivial bands near $m_z^c = \pm 0.44E_r$, according to the theory in (*33*), which agrees with the experimental observation. Note that around $m_z = 0$, the spin polarizations at $X_{1,2}$ change sign through zero, implying the gap closing at $X_{1,2}$ and a change of Chern number by 2. This confirms that for the 2D SO-coupled system realized in the present experiment, the energy band is topologically nontrivial when $0 < |m_z| < |m_z^c|$, whereas it is trivial for $|m_z| > |m_z^c|$.

Estimation of heating

The heating rate of the dipole trap is measured to be 18 nK/s, mainly owing to the photon scattering and the intensity noise. This results in a BEC lifetime of about 10 s. The heating rate of the lattice and the Raman lights caused by photon scattering is about four times that of the dipole trap, in the regime for $V_0 = 4.16E_r$ and $M_0 = 1.32E_r$ (*32*). Nevertheless, in the current experiment, residual heating is induced by the fluctuation of the bias magnetic field, which drives additional spin-flip dynamics in the presence of resonant Raman couplings. This contribution to the heating is about one order higher that of the dipole trap, reducing the lifetime of the SO-coupled BEC to just above 300 ms. This lifetime is sufficient to explore both single-particle and interacting physics for the ^{87}Rb BEC system. Moreover, stabilizing the bias magnetic field may result in an even longer lifetime of seconds in appropriate parameter regimes.

Discussion and outlook

The 2D SO coupling we realized here is for real spins (hyperfine eigenstates) of atoms, which can be precisely measured and engineered experimentally. In comparison, a 2D SO coupling via a tripod system (*7*, *24*, *27*) or ring-coupling scheme (*25*) corresponds to pseudospins defined by superpositions of multiple hyperfine levels with superposition coefficients being spatially dependent. This conceptual difference manifests the advantages of the present realization for future broad studies of SO effects and interacting physics. Furthermore, owing to the realization in the optical lattice, the present 2D SO coupling can bring about much richer physics than a pure 2D Rashba correspondence. In the s-band regime, the present Bloch Hamiltonian describes a quantum anomalous Hall model driven by SO coupling, which cannot be exactly realized in solid-state materials. Thus, even in the single-particle regime, our realization leads to nontrivial topological bands, whereas a single-particle 2D Rashba system is topologically trivial. Moreover, even richer physics can be obtained if considering the higher-band (e.g., p-band) regimes.

Many experimental studies—including the measurement of topological Hall effects, Berry phase mechanism, and k-space monopole—can be performed on the basis of the present realization. On the other hand, with the high controllability of the present realization, the SO interaction can be readily switched on and off and can be adjusted between 1D and 2D limits. This may lead to rich quench spin dynamics in the optical lattice with nontrivial band topology. Moreover, with the present SO coupling in the optical lattice, one may explore states of matter [such as SO-coupled Mott insulators with interacting bosons (*35*, *36*)] that have no analog in solids.

Furthermore, the present optical Raman lattice scheme is generic and can be immediately applied to fermion systems (e.g., ^{40}K), in which case, the quantum anomalous Hall effect in the single-particle regime and topological superfluid (*28*) or novel magnetic phases (*37*) in the interacting regimes will be especially noteworthy. In particular, the topological superfluid phase is highly sought after because it hosts Majorana quasiparticles, which obey non-Abelian statistics (*38*) and have attracted attention in both condensed matter and cold atom physics (*5*). Finally, although the present study is focused on a 2D lattice system, generalizing our scheme to 3D optical lattices may lead to the realization of topological phases in 3D systems, including the Weyl topological semimetals (*39*, *40*).

REFERENCES AND NOTES

1. M. Z. Hasan, C. L. Kane, *Rev. Mod. Phys.* **82**, 3045–3067 (2010).
2. X.-L. Qi, S.-C. Zhang, *Rev. Mod. Phys.* **83**, 1057–1110 (2011).
3. N. Read, D. Green, *Phys. Rev. B* **61**, 10267–10297 (2000).
4. A. Y. Kitaev, *Phys. Uspekhi* **44**, 131–136 (2001).
5. F. Wilczek, *Nat. Phys.* **5**, 614–618 (2009).
6. J. Alicea, *Rep. Prog. Phys.* **75**, 076501 (2012).
7. J. Ruseckas, G. Juzeliūnas, P. Öhberg, M. Fleischhauer, *Phys. Rev. Lett.* **95**, 010404 (2005).
8. K. Osterloh, M. Baig, L. Santos, P. Zoller, M. Lewenstein, *Phys. Rev. Lett.* **95**, 010403 (2005).
9. X.-J. Liu, M. F. Borunda, X. Liu, J. Sinova, *Phys. Rev. Lett.* **102**, 046402 (2009).
10. Y.-J. Lin, K. Jiménez-García, I. B. Spielman, *Nature* **471**, 83–86 (2011).
11. J.-Y. Zhang *et al.*, *Phys. Rev. Lett.* **109**, 115301 (2012).
12. P. Wang *et al.*, *Phys. Rev. Lett.* **109**, 095301 (2012).
13. L. W. Cheuk *et al.*, *Phys. Rev. Lett.* **109**, 095302 (2012).
14. K. Jiménez-García *et al.*, *Phys. Rev. Lett.* **108**, 225303 (2012).
15. C. Wang, C. Gao, C.-M. Jian, H. Zhai, *Phys. Rev. Lett.* **105**, 160403 (2010).
16. C.-J. Wu, I. Mondragon-Shem, X.-F. Zhou, *Chin. Phys. Lett.* **28**, 097102 (2011).
17. T.-L. Ho, S. Zhang, *Phys. Rev. Lett.* **107**, 150403 (2011).
18. S.-C. Ji *et al.*, *Nat. Phys.* **10**, 314–320 (2014).
19. V. Galitski, I. B. Spielman, *Nature* **494**, 49–54 (2013).
20. T. F. J. Poon, X.-J. Liu, *Phys. Rev. A* **93**, 063420 (2016).
21. N. Goldman, G. Juzeliūnas, P. Öhberg, I. B. Spielman, *Rep. Prog. Phys.* **77**, 126401 (2014).
22. C. Zhang, S. Tewari, R. M. Lutchyn, S. Das Sarma, *Phys. Rev. Lett.* **101**, 160401 (2008).
23. M. Sato, Y. Takahashi, S. Fujimoto, *Phys. Rev. Lett.* **103**, 020401 (2009).
24. C. Zhang, *Phys. Rev. A* **82**, 021607(R) (2010).
25. D. L. Campbell, G. Juzeliūnas, I. B. Spielman, *Phys. Rev. A* **84**, 025602 (2011).
26. N. R. Cooper, *Phys. Rev. Lett.* **106**, 175301 (2011).
27. L. Huang *et al.*, *Nat. Phys.* **12**, 540–544 (2016).
28. X.-J. Liu, K. T. Law, T. K. Ng, *Phys. Rev. Lett.* **112**, 086401 (2014).
29. M. Aidelsburger *et al.*, *Phys. Rev. Lett.* **111**, 185301 (2013).
30. H. Miyake, G. A. Siviloglou, C. J. Kennedy, W. C. Burton, W. Ketterle, *Phys. Rev. Lett.* **111**, 185302 (2013).
31. M. Aidelsburger *et al.*, *Nat. Phys.* **11**, 162–166 (2015).
32. See supplementary materials for more details about model realization, SO coupling, nontrivial topological bands, band topological measurement, and estimation of heating.
33. X.-J. Liu, K. T. Law, T. K. Ng, P. A. Lee, *Phys. Rev. Lett.* **111**, 120402 (2013).
34. S.-C. Ji *et al.*, *Phys. Rev. Lett.* **114**, 105301 (2015).
35. Z. Cai, X. Zhou, C. Wu, *Phys. Rev. A* **85**, 061605(R) (2012).
36. W.-S. Cole, S. Zhang, A. Paramekanti, N. Trivedi, *Phys. Rev. Lett.* **109**, 085302 (2012).
37. J. Radić, A. Di Ciolo, K. Sun, V. Galitski, *Phys. Rev. Lett.* **109**, 085303 (2012).
38. D. A. Ivanov, *Phys. Rev. Lett.* **86**, 268–271 (2001).
39. S.-Y. Xu *et al.*, *Science* **349**, 613–617 (2015).
40. H. Weng, C. Fang, Z. Fang, B. A. Bernevig, X. Dai, *Phys. Rev. X* **5**, 011029 (2015).

ACKNOWLEDGMENTS

We thank J. Ho, T.-F. J. Poon, and G.-B. Jo for helpful discussions. This work has been supported by the Ministry of Science and Technology of China (under grants 2016YFA0301601 and 2016YFA0301604), National Natural Science Foundation of China, the CAS, the National Fundamental Research Program (under grant 2013CB922001), Fundamental Research Funds for the Central Universities (under grants 2030020028 and 2340000034), and Peking University Initiative Scientific Research Program. X.-J.L. acknowledges support from the National Natural Science Foundation of China (grant 11574008). X.-J.L. and L.Z. are also supported by the Thousand-Young-Talent Program of China.

SUPPLEMENTARY MATERIALS

www.sciencemag.org/content/354/6308/83/suppl/DC1
Supplementary Text
Figs. S1 to S6
References (*41*, *42*)

11 March 2016; accepted 12 September 2016
10.1126/science.aaf6689

REPORTS

GEOPHYSICS

Localized seismic deformation in the upper mantle revealed by dense seismic arrays

Asaf Inbal,* Jean Paul Ampuero, Robert W. Clayton

Seismicity along continental transform faults is usually confined to the upper half of the crust, but the Newport-Inglewood fault (NIF), a major fault traversing the Los Angeles basin, is seismically active down to the upper mantle. We use seismic array analysis to illuminate the seismogenic root of the NIF beneath Long Beach, California, and identify seismicity in an actively deforming localized zone penetrating the lithospheric mantle. Deep earthquakes, which are spatially correlated with geochemical evidence of a fluid pathway from the mantle, as well as with a sharp vertical offset in the lithosphere-asthenosphere boundary, exhibit narrow size distribution and weak temporal clustering. We attribute these characteristics to a transition from strong to weak interaction regimes in a system of seismic asperities embedded in a ductile fault zone matrix.

Earthquakes occurring along transform plate boundaries are generally confined to the upper portions of the crust, with upper mantle deformation being predominantly aseismic (*1*). Seismological investigations of active faulting at lower crustal depths are limited by highly attenuated signals whose level barely exceeds the noise at Earth's surface, and by the sparseness of regional seismic networks. Consequently, important physical parameters characterizing the transition from brittle fracture to ductile flow at the base of the seismogenic zone are generally very poorly determined (*2*).

Because seismic tomography usually cannot resolve features whose spatial extent is less than about 10 km in the mid-lower crust (*3*–*5*), the

Seismological Laboratory, California Institute of Technology, Pasadena, CA 91125, USA.
*Corresponding author. Email: ainbal@gps.caltech.edu

Realization of two-dimensional spin-orbit coupling for Bose-Einstein condensates

Zhan Wu, Long Zhang, Wei Sun, Xiao-Tian Xu, Bao-Zong Wang, Si-Cong Ji, Youjin Deng, Shuai Chen, Xiong-Jun Liu and Jian-Wei Pan (October 6, 2016)

Science **354** (6308), 83-88. [doi: 10.1126/science.aaf6689]

Editor's Summary

Spin-orbit coupling in an optical lattice

Studying topological matter in cold-atom systems may bring fresh insights, thanks to the intrinsic purity and controllability of this experimental setting. However, the necessary spin-orbit coupling can be tricky to engineer. Wu *et al.* conceived and experimentally demonstrated a simple scheme that involves only a single laser source and can be continuously tuned between one- and two-dimensional spin-orbit coupling (see the Perspective by Aidelsburger). Although this experiment used bosonic atoms, it is expected that the setup would also work for fermions.

Science, this issue p. 83; see also p. 35